AAS 18-361

PLANAR ORBIT AND ATTITUDE DYNAMICS OF AN EARTH-ORBITING SOLAR SAIL UNDER J_2 AND ATMOSPHERIC DRAG EFFECTS

Narcís Miguel and Camilla Colombo*

In this paper we study planar orbit and attitude dynamics of an uncontrolled spacecraft taking on-board a deorbiting device such as a drag or solar sail. The dynamics is studied in mean Keplerian elements and restricted to rotations around one of the principal axes of the spacecraft. We consider spacecraft with a simplified version of a solar sail with pyramidal shape to restrict ourselves to planar motion, and we investigate stable or slowly-varying attitudes affected by disturbances due to the Earth oblateness effect, solar radiation pressure, and atmospheric drag, with special emphasis on orbits above 800 km of altitude. A sensitivity analysis on the aperture of the sail is performed.

INTRODUCTION

Solar sails are a low-thrust propulsion that relies on the Solar Radiation Pressure (SRP). They have attracted much attention in the literature, since a spacecraft with a solar sail generated acceleration in a slow but continuous way allowing to reduce the cost of missions. This technology has been successfully demonstrated in various missions, see for instance JAXA's IKAROS,[1] the Planetary Society's LightSail projects and NASA's NanoSail-D project.[2] The latter demonstrated the feasibility of the deployment of a sail and its usage to deorbit a spacecraft exploiting the effect of atmospheric drag.

There is a vast literature on how to use the enhancements of the effects of SRP and drag for mission design. A common feature among these works is to assume that, along the trajectories, the attitude of the sail is fixed; hence the feasibility of these works rely on attitude control.

In this work and we build on studies whose objectives are end-of-life disposals employing sails as passive deorbiting devices. For deorbiting from an altitude where atmospheric drag is the dominant effect, the sail can be either controlled, to keep always its maximum cross area perpendicular to the incoming air flow, or uncontrolled and therefore tumbling. In this case the cross area exposed to aerodynamic drag will be varying in time.[3] For orbit altitude above 800 km, the effect of SRP can be exploited for achieve deorbiting. Deorbiting strategies making use of SRP can be splitted in two main attitude control strategies, active and passive, as defined in.[4] Active strategies allow deorbiting "inwards" on a spiraling path by decreasing the semi-major axis of the orbit. This is achieved by maximizing the SRP effect when approaching the Sun and minimizing it when moving away from the Sun,[5] see the left panel in Figure 1. On the other hand, the passive approach requires a fixed attitude of the spacecraft with respect to the Sun, and it consists of the counter-intuitive idea

* Department of Aerospace Science and Technology, Politecnico di Milano, 20156 Milano MI, Italy.
E-mail: narcis.miguel@polimi.it; camilla.colombo@polimi.it.

of deorbiting "outwards" by increasing the eccentricity of the orbit, since this implies the decrease of the perigee,[6,7] see the right panel in Figure 1.

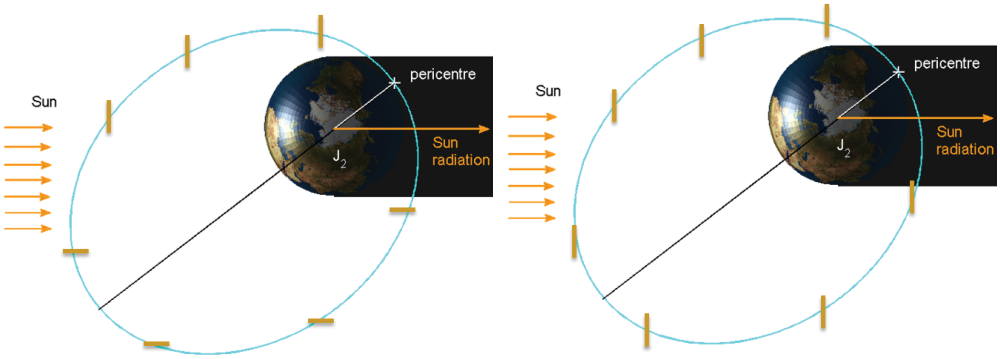

Figure 1. Sail orientation in the active (left) and the passive (right) deorbiting strategies.[4]

Here the natural question arises whether one can find a sail with auto-stabilizing properties, so that the already cited strategies can apply minimizing the need for attitude control. The answer is affirmative from the point of view of SRP, and it is achieved by means of a quasi-rhombic pyramid (QRP) shape, as suggested in.[8] The structure is formed by 4 reflective panels resembling the shape of the pyramid. If oriented towards the sunlight, such a structure is expected to compensate, on average, the components of the acceleration in any other direction. Namely, in[9] the authors provide a first-order (and hence local) argument for the stability of the sun-pointing attitude, and they later study the possible stability enhancements of assuming a moderate spin around this direction in.[10]

Despite the authors of[8,9,10] obtain satisfactory results by considering such structure, there is, to the author's knowledge, a lack of understanding on the stability from a more global point of view. That is, if there are also stable attitude dynamics close to the sun-pointing orientation, and, in affirmative case, if one can measure and describe the set of stable motion. This paper is a first step in this direction.

The goal of this paper is to give a deterministic model of the attitude dynamics that allows to quantitatively study up to which extent the QRP is stable. As a first approximation, we consider the problem to be planar and that the direction of the sunlight is the Sun-Earth vector. To avoid out-of-plane motion, we set the ecliptic obliquity to be zero and consider a simplified version of the QRP sail that only consists of two panels. This also allows to consider a variable position of the bus with respect to the sail, and to perform a sensitivity analysis with respect to this distance and the aperture of the sail panels.

The first section is devoted to the study of the geometry of the spacecrafts under consideration and to provide their inertia moments. These depend on the aperture angle and position of the bus with respect to the sail structure. Since we only consider planar motion, the rotation dynamics only happens around the direction perpendicular to the orbital plane. In the following section we provide explicit expressions for the SRP and gravity gradient torques. An expression of the torque due to atmospheric drag is also provided by taking into account that it is analogous to the SRP torque, but where the vector opposite to the velocity of the spacecraft plays the role of the direction of the sunlight.

After this, we can set and study a simplified deterministic model for the attitude dynamics in the presence of SRP and gravity gradient torques, that consists of assuming that the dynamics happens on a fixed Keplerian orbit and that the apparent motion of the Sun around the Earth is on a circular orbit. Reflecting on well known mathematical models, we give criteria for the stability of the sun-pointing direction and study numerically its vicinity, where non-negligible regions of stable motion can be detected. The results of the simplified model are confirmed with simulations of a complete orbit and attitude model that considers the accelerations due to SRP and the J_2 effect.

Then the analogous drag and gravity-gradient torque case is considered. The similarities between SRP and drag allow to translate some of the previous analytical studies, but in this situation, the fact that the attitude depends so strongly on the orbit does not allow to set any deterministic simplified model, yet the stability of the velocity-pointing orientation can be established similarly. Here we are led directly to the study the problem considering the corresponding complete orbit and attitude model.

We finish by summarizing the obtained results and giving some examples of future lines of research that emerge from this contribution.

GEOMETRY OF THE SAIL

To avoid out-of-plane motion we are lead to consider a sail structure that consists of two panels of equal size, of height h, width w, and area $A_s = hw$. Assume that the weight of each panel is $m_s/2$, so the mass of the whole sail structure is m_s. In the left panel of Fig. 2 a sketch of the sail structure is depicted.

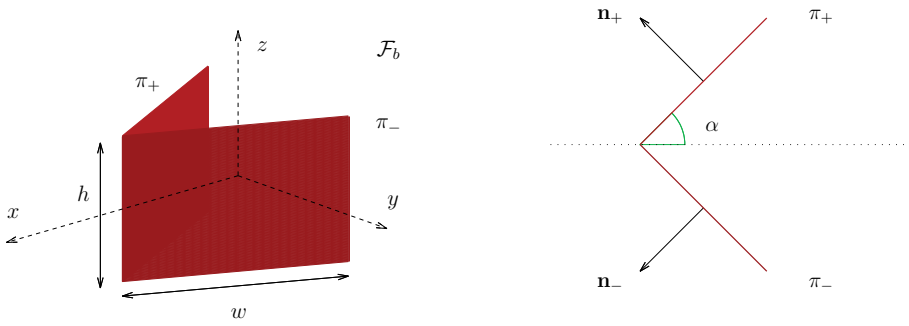

Figure 2. Sketch of the sail structure. Left: 3D view. Right: top view.

The parametrization of the sail is written in a reference frame $\mathcal{F}_b$ attached to the spacecraft whose coordinates are x, y and z. Call $\mathbf{i}_{x,y,z}$ the vectors of the basis. Consider cylindrical coordinates (r, α, z), $r = x^2 + y^2$ and $\tan\alpha = y/x$. The panels of the sail are parametrized as

$$\text{Sail}: \qquad \pi_+ \cup \pi_-, \quad \pi_\pm = \left\{ (\texttt{aux} - r\cos\alpha, \pm r\sin\alpha, z)^\top : \ r \in [0, w], \ z \in [-h/2, h/2] \right\} \quad (1)$$

where aux is a free parameter that will be chosen so that the center of mass of the whole spacecraft is at the origin of $\mathcal{F}_b$. The panels are attached to each other along an h-long side, that lies on a line parallel to the z axis, and they form an angle α with respect to the plane $y = 0$. Assuming uniform density of the sail, the centre of mass of the structure is at

$$\mathbf{r}_s = \left(\texttt{aux} - \frac{1}{2} w\cos\alpha, 0, 0 \right)^\top.$$

Note that chosen this way, the principal axes of inertia of the sail are parallel to those of $\mathcal{F}_b$. This property remains true if the center of mass of the bus of the satellite lies on the x axis. So, assume that it is located at the point $\mathbf{r}_s + (d, 0, 0)^\top$, $d \in \mathbb{R}$. Here d is considered to be a parameter of the problem that measures the distance between centres of mass of the bus and sail structure. As we will see later on, d plays a role both in the stability and in the inertia moments along the x and z axes: the larger $|d|$, the larger these inertia moments are. It is easy to check that the centre of mass of the whole spacecraft is the origin if we choose

$$\texttt{aux} \quad = \quad \frac{1}{2} w \cos\alpha - d \frac{m_b}{m_b + m_s}, \tag{2}$$

where m_b is the mass of the bus. Sketches of top views of spacecraft in $\mathcal{F}_b$ can be seen in Fig. 3, where we represent the bus as a solid black dot. The left panel displays a bus with $d = 0$. Any spacecraft with $d < 0$ has the bus further to the left. The center panel displays a case where $d > 0$ and the bus is at the tip of the sail structure. Finally in the right panel one can see an example of spacecraft with bus completely in front of the sail structure.

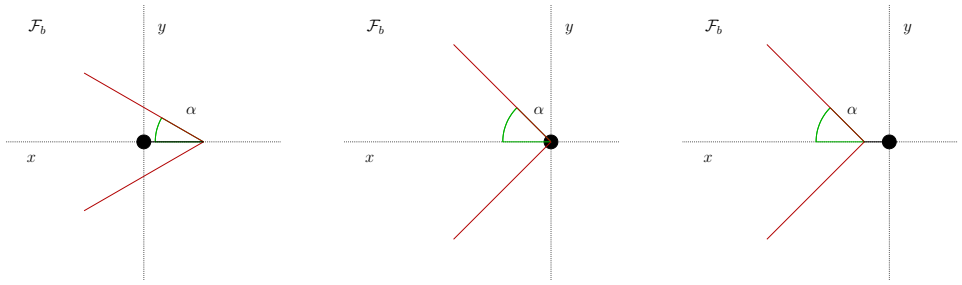

Figure 3. Sketch of the top view of the spacecraft in $\mathcal{F}_b$, where the bus is depicted as a solid circle. Left: $d = 0$. Center: $d > 0$ with the bus at the tip of the sail structure. Right: $d > 0$ with the bus in front of the sail structure.

Assume that the principal axes of the bus are also parallel to the axes of $\mathcal{F}_b$, and denote $I_{x,b}, I_{y,b}$ and $I_{z,b}$ its moments of inertia if its centre of mass is at the origin. Using the parallel axes theorem, the moments of inertia along the x, y and z axes of the whole spacecraft are, respectively,

$$A = I_{x,b} + \frac{h^2 m_s}{6}, \quad B = I_{y,b} + \frac{h^2 m_s}{6} + D(\alpha, d), \quad C = I_{z,b} + D(\alpha, d), \tag{3}$$

$$D(\alpha, d) \quad = \quad \frac{1}{6} m_s w^2 \cos^2\alpha + \frac{d^2 m_b^2 (m_b + 2m_s)}{(m_b + m_s)^2} \tag{4}$$

Finally, denote $\mathbf{n}_\pm = (\sin\alpha, \pm\cos\alpha, 0)$ the normal vector of the panels $\pi_\pm$, see the right sketch in Fig. 2.

MODEL OF PLANAR ORBIT AND ATTITUDE DYNAMICS

The planar orbit and attitude dynamics we consider is a coupled system of differential equations in $\mathbb{R}^6$: orientation and angular velocity for the attitude and the variation of the semi-major axis a,

eccentricity e, the sum of the argument of the perigee ω and the right ascension of the ascending node or RAAN Ω, and true anomaly for the orbit, f. The variational equation of the RAAN is added to account for the nodal precession, that occurs due to the J_2 acceleration.

Since we are dealing with planar motion, the rotation dynamics of the spacecraft is fully explained using a single Euler angle, $\varphi \in [0, 2\pi)$, and the Euler equations in this situation reduce to

$$C\ddot{\varphi} \;=\; \mathbf{M}_3 \qquad \text{or} \qquad \left\{ \begin{array}{rcl} \dot{\varphi} & = & \Phi \\ \dot{\Phi} & = & \mathbf{M}_3/C \end{array} \right. , \tag{5}$$

where Φ is the rotational angular velocity and C is the third inertia moment, recall Eq. 3, and $\mathbf{M}_3$ refers to the sum of the components along the z direction of the torques under consideration, that will be derived in the next subsection. Hence the state vector of the complete problem will be of the form

$$[\varphi,\ \Phi,\ a,\ e,\ \omega + \Omega,\ f]^\top .$$

Attitude dynamics

Let $\mathbf{M}$ denote the torque due to external forces acting on the body. Here we consider that either $\mathbf{M} = \mathbf{M}_{\rm SRP} + \mathbf{M}_{\rm GG}$, or $\mathbf{M} = \mathbf{M}_{\rm drag} + \mathbf{M}_{\rm GG}$. That is, the total torque is the sum of the effects due to gravity gradient with either solar radiation pressure or atmospheric drag.

To provide explicit expressions of the considered torques, we need to write the Sun-Earth, Earth-spacecraft vectors and the relative velocity of the spacecraft with the atmosphere in the reference frame $\mathcal{F}_b$. Denote them, respectively, as

$$\mathbf{u}_{\rm S} \;=\; \sigma_1\mathbf{i}_x + \sigma_2\mathbf{i}_y + \sigma_3\mathbf{i}_z, \quad \mathbf{r}_{\rm S} = r_{\rm S}\mathbf{u}_{\rm S}, \tag{6a}$$

$$\mathbf{u}_{\rm E} \;=\; \gamma_1\mathbf{i}_x + \gamma_2\mathbf{i}_y + \gamma_3\mathbf{i}_z, \quad \mathbf{r}_{\rm E} = r_{\rm E}\mathbf{u}_{\rm E}. \tag{6b}$$

$$\mathbf{u}_{\rm rel} \;=\; \nu_1\mathbf{i}_x + \nu_2\mathbf{i}_y + \nu_3\mathbf{i}_z, \quad \mathbf{v}_{\rm rel} = v_{\rm rel}\mathbf{u}_{\rm rel}, \tag{6c}$$

where

$$\sigma_1^2 + \sigma_2^2 + \sigma_3^2 \;=\; \gamma_1^2 + \gamma_2^2 + \gamma_3^2 \;=\; \nu_1^2 + \nu_2^2 + \nu_3^2 \;=\; 1$$

are direction cosines. All the vectors in Eq. 6 will only be referred to in the the $\mathcal{F}_b$ frame, so there is no risk of confusion by not specifying the frame in which the cosines are defined. Since we are only considering rotations around the z axis to force the motion to be in the ecliptic plane, we only need formulas for the third component of each of the torques.

Solar radiation pressure The force due to SRP exerted in each panel of the sail is[11]

$$\mathbf{F}^{\pm}_{\rm SRP} \;=\; p_{\rm SR} A_s (n_\pm \cdot \mathbf{u}_{\rm S}) \left(2\eta(n_\pm \cdot \mathbf{u}_{\rm S})n_\pm + (1-\eta)\mathbf{u}_{\rm S}\right), \tag{7}$$

where $\eta \in (0,1)$ is the (dimensionless) reflectance of the sail and $p_{\rm SR} = 4.56 \times 10^{-6}\ \mathrm{N/m^2}$ is the solar pressure at 1 AU which is considered to be constant. The torque due to SRP is, hence, $\mathbf{M}_{\rm SRP} = \mathbf{M}^-_{\rm SRP} + \mathbf{M}^+_{\rm SRP}$, where $\mathbf{M}^{\pm}_{\rm SRP} = \mathbf{r}_\pm \times \mathbf{F}^{\pm}_{\rm SRP}$, and $\mathbf{r}_\pm$ is the location of the center of mass of the sail panel $\pi_\pm$. Their third component $\mathbf{M}^{\pm}_{{\rm SRP},3}$ read

$$\mathbf{M}^{\pm}_{{\rm SRP},3} \;=\; \frac{A_s}{m_b + m_s}\frac{p_{\rm SR}}{2}\left(a_{1,1}(\eta)\sigma_1\sigma_2 \pm a_{2,0}(\eta)\sigma_1^2 \pm a_{0,2}(\eta)\sigma_2^2\right), \tag{8}$$

where

$$
\begin{aligned}
a_{1,1}(\eta) &= -\sin\alpha\left[2dm_b(2\eta\cos(2\alpha)+\eta+1)+w(m_b+m_s)(\cos\alpha-\eta\cos(3\alpha))\right], && \text{(9a)}\\
a_{2,0}(\eta) &= -\sin^2\alpha\left[4d\eta m_b\cos\alpha+w(m_b+m_s)(1-\eta\cos(2\alpha))\right], \text{ and} && \text{(9b)}\\
a_{0,2}(\eta) &= -\cos\alpha\left[2dm_b(\eta\cos(2\alpha)+1)+\eta w(m_b+m_s)\sin\alpha\sin(2\alpha)\right]. && \text{(9c)}
\end{aligned}
$$

In view of the scope of this contribution it is reasonable to assume that the sail panels have a black non-reflective back side. Hence, the SRP torque can be due to the effect of 0 (no torque), 1 or 2 panels. In case the two panels face the sunlight one obtains the simplified expression

$$
\mathbf{M}_{\mathrm{SRP},3} = \frac{A_s}{m_b+m_s}p_{\mathrm{SR}}a_{1,1}(\eta)\sigma_1\sigma_2. \tag{10}
$$

The coefficients $a_{1,1}, a_{2,0}$ and $a_{0,2}$ also depend on the masses m_b, m_s, the parameters α, d and the width w, but we only stress the dependence on η for reasons that will be clear when dealing with the torque due to atmospheric drag.

Gravity gradient The rotation of asymmetrical bodies are affected by a torque due to gravity gradient that can be written as[11]

$$
\mathbf{M}_{\mathrm{GG}} = \frac{3\mu}{r_{\mathrm{E}}^3}\mathbf{u}_{\mathrm{E}}\times\mathbf{I}_{\mathrm{sc}}\mathbf{u}_{\mathrm{E}},
$$

where $\mu = GM_{\mathrm{E}} = 3.986\times10^{14}\ \mathrm{m}^3/\mathrm{s}^2$ is the gravitational parameter of the Earth and $\mathbf{I}_{\mathrm{sc}} = \mathrm{diag}(A,B,C)$ is the inertia tensor of the spacecraft. Its component in the z direction is

$$
\mathbf{M}_{\mathrm{GG},3} = \frac{3\mu}{r_{\mathrm{E}}^3}(B-A)\gamma_1\gamma_2 = \frac{3\mu}{r_{\mathrm{E}}^3}\left(I_{y,b}-I_{x,b}+D(\alpha,d)\right)\gamma_1\gamma_2, \tag{11}
$$

recall Eq. 4. In practice we assume a symmetric bus, so the factor in the parenthesis of the right hand side in Eq. 11 reduces to $D(\alpha,d)$.

Atmospheric drag The force due to atmospheric drag can be decomposed as the sum of the forces to exerted to each of the two panels, that can be written as[11]

$$
\mathbf{F}_{\mathrm{drag}}^{\pm} = -\frac{1}{2}\rho v_{\mathrm{rel}}^2 C_D A_s(\mathbf{n}_{\pm}\cdot\mathbf{u}_{\mathrm{rel}})\mathbf{u}_{\mathrm{rel}}, \tag{12}
$$

where ρ is the atmospheric density and $C_D\in(1.5,2.5)$ is an empirically determined dimensionless drag coefficient. The torque due to this force is, hence, $\mathbf{M}_{\mathrm{drag}} = \mathbf{r}_-\times\mathbf{F}_{\mathrm{drag}}^- + \mathbf{r}_+\times\mathbf{F}_{\mathrm{drag}}^+$, where $\mathbf{r}_\pm$ is the location of the centre of mass of the sail panel $\pi_\pm$, and

$$
\mathbf{M}_{\mathrm{drag},3}^{\pm} = \frac{A_s}{m_b+m_s}\frac{\rho v_{\mathrm{rel}}^2 C_D}{4}\left(b_{1,1}\nu_1\nu_2 \pm b_{2,0}\nu_1^2 \pm b_{0,2}\nu_2^2\right), \tag{13}
$$

where

$$
\begin{aligned}
b_{1,1} &= -\sin\alpha\left[2dm_b + wm_b\cos\alpha\right], && \text{(14a)}\\
b_{2,0} &= -\sin^2\alpha\left[w(m_b+m_s)\right], \text{ and} && \text{(14b)}\\
b_{0,2} &= -\cos\alpha\left[2dm_b\right]. && \text{(14c)}
\end{aligned}
$$

Note that Eq. 14 and Eqs. 9 are related: $b_{1,1} = a_{1,1}(0)$, $b_{2,0} = a_{2,0}(0)$ and $b_{0,2} = a_{0,2}(0)$.

We are only interested in the orientations of the sail where the torque due to atmospheric drag could be due to either 1 or two panels. In case the two panels face the atmosphere and hence produce torque the obtained expression is the sum of $\mathbf{M}^{\pm}_{\mathrm{drag},3}$, that reads

$$\mathbf{M}_{\mathrm{drag},3} = \frac{A_s}{m_b + m_s}\frac{\rho v_{\mathrm{rel}}^2 C_D}{2} a_{1,1}(0)\nu_1\nu_2, \tag{15}$$

compare with Eq. 10.

Orbit dynamics

The orbit dynamics are propagated in the form of Gauss' variational equations. Since we deal with the effect of atmospheric drag, it is convenient to consider them in a tangential-normal frame: $\mathcal{F}_{\mathrm{t,n,h}}$, whose vectors of the orthonormal basis are $\mathbf{i}_{\mathrm{t,n,h}}$. Since we are dealing with planar motion, $\mathbf{i}_z$ and $\mathbf{i}_{\mathrm{h}}$ are parallel vectors. The vector $\mathbf{i}_{\mathrm{t}}$ is parallel to the velocity vector oriented towards the motion and the triad is completed by choosing $\mathbf{i}_{\mathrm{n}} = \mathbf{i}_{\mathrm{h}} \times \mathbf{i}_{\mathrm{t}}$. In this frame, the variational equations are[12]

$$\frac{d\Omega}{dt} = -\frac{3}{h}\frac{J_2 \mu R_E^2}{r^3}\sin^2(\omega + f), \tag{16a}$$

$$\frac{da}{dt} = \frac{2a^2 v}{\mu} a_{\mathrm{t}}, \tag{16b}$$

$$\frac{de}{dt} = \frac{1}{v}\left[2(e + \cos f)a_{\mathrm{t}} - \frac{r}{a}\sin f a_{\mathrm{n}}\right], \tag{16c}$$

$$\frac{d\omega}{dt} = \frac{1}{ev}\left[2\sin f a_{\mathrm{t}} + \left(2e + \frac{r}{a}\cos f\right) a_{\mathrm{n}}\right] - \frac{d\Omega}{dt}, \tag{16d}$$

$$\frac{df}{dt} = \frac{h}{r^2} - \frac{1}{ev}\left[2\sin f a_{\mathrm{t}} + \left(2e + \frac{r}{a}\cos f\right) a_{\mathrm{n}}\right], \tag{16e}$$

where $h = na^2\sqrt{1-e^2}$ and $n = \sqrt{\mu/a^3}$ is the mean motion. Since the only out-of-plane effect is that of J_2 along $\mathbf{i}_{\mathrm{h}}$ we have already made it explicit in the equations of the orbit. Note that the second summand of Eq. 16d is the right hand side of Eq. 16a. This is a special feature of the present simplified planar models since the inclination is zero.

The terms a_{t} and a_{n} are the components of the total disturbing acceleration in the direction of $\mathbf{i}_{\mathrm{t}}$ and $\mathbf{i}_{\mathrm{n}}$, respectively. This disturbing acceleration is found via Eq. 7 for SRP and Eq. 12 for the atmospheric drag simply dividing them by the spacecraft mass. Concerning the acceleration due to the oblateness of the Earth, the components can be found via the disturbing function

$$R = -\frac{\mu J_2 R_E}{2r^3}\left[3\sin^2 i \sin^2(\omega + f) - 1\right],$$

see, e.g., Battin,[12] p. 503.

Study cases of the simulations

There are some aspects of the dynamics that can be studied analytically and some features can be explained via arguments from the theory of dynamical systems. But the complete system depends on many independent parameters that account for the size, shape, materials, etc. of the spacecraft. Some of these free independent parameters can be related to each other if we impose that the spacecraft under study is feasible according to current technological constraints. In[13] the authors provide

a way to check if, given m_b and an area-to-mass ratio, it is feasible to construct a solar sail with these requirements, and they provide a way to obtain the side-length of such a (square) sail, and which should be its mass.

To exemplify the results of this work, we consider spacecrafts formed of two equal square panels as in the sketch in Fig. 2, with reflectance $\eta = 0.8$, and we have obtained its measurements by assuming the conservative values $m_b = 100$ kg, $w = h = 9.20$ m and $m_s = 3.60$ kg, that give rise to an area-to-mass ratio $A_s/(m_b + m_s) \approx 0.75$ m^2/kg.

Since the results depend strongly on the physical parameters α and d, we have studied the dynamics of 2 structures: $\mathtt{SC}_1$, with $\alpha = 30°$ and $d = 0$ m, and $\mathtt{SC}_2$, with $\alpha = 45°$ and $d = 2.9$ m. In the left and center panels of Fig. 3 sketches of top views of $\mathtt{SC}_1$ and $\mathtt{SC}_2$ are shown, respectively. These spacecraft are characterized by the fact that in $\mathtt{SC}_1$ the centres of mass of the bus and the sail structure are at the origin, and in $\mathtt{SC}_2$ the bus is at the tip of the sail, as suggested in.[8] In Tab. 1 we provide some relevant physical parameters of the two sails, obtained by assuming a symmetric cubic bus of side-length 1 m.

		$\mathtt{SC}_1$: $\alpha = 30°$, $d = 0$ m	$\mathtt{SC}_2$: $\alpha = 45°$, $d = 2.90$ m
A	[kg km^2]	6.74506667e-05	6.74506667e-05
B	[kg km^2]	1.05538667e-04	9.32827163e-04
C	[kg km^2]	5.47546667e-05	8.82043163e-04
$a_{1,1}(0.8)$	[kg km]	4.12713066e-01	1.59602748e+00
$a_{2,0}(0.8)$	[kg km]	1.42968000e-01	8.04657546e-01
$a_{0,2}(0.8)$	[kg km]	2.85936000e-01	7.91369933e-01
$b_{1,1}$	[kg km]	4.12713066e-01	8.86681933e-01
$b_{2,0}$	[kg km]	2.38279999e-01	4.76560000e-01
$b_{0,2}$	[kg km]	0.00000000e+00	4.10121933e-01

Table 1. Physical parameters of the two structures $\mathtt{SC}_1$ and $\mathtt{SC}_2$.

STABILIZING PROPERTIES IN A SRP-DOMINATED REGION

In this section we deal with the auto-stabilizing properties of the sail sketched in Fig. 2 under the effect of SRP and gravity-gradient only. A very important feature of this effect is that, if we consider the sunlight direction to be the Sun-Earth vector, the representation of the torque in Eq. 8 does not depend on the orbit. Hence, the gravity-gradient torque, Eq. 11 can be considered a perturbation whose size is proportional to a^{-3}.

The dynamics we are interested in requires the definition of two additional reference frames. We consider an inertial frame $\mathcal{F}_I$ centered in the position of the Earth, with coordinates X, Y and Z. Denote the vectors of the orthonormal basis $\mathbf{i}_{X,Y,Z}$. Since we are dealing with the planar problem, the vectors $\mathbf{i}_z$ and $\mathbf{i}_Z$ are parallel. The triad is completed by choosing $\mathbf{i}_Y = \mathbf{i}_Z \times \mathbf{i}_X$.

Since here we study the coupled effect of SRP and the gravity gradient, it is convenient to follow the position of the spacecraft along its orbit with a polar reference frame $\mathcal{F}_{r,\theta,h}$, with coordinates r, θ, h. Denote the vectors of the orthonormal basis $\mathbf{i}_{r,\theta,h}$. The $\mathbf{i}_r$ direction is that of the position of the spacecraft, $\mathbf{i}_h$ is normal to the orbital plane (hence parallel to $\mathbf{i}_z$ and $\mathbf{i}_Z$) and $\mathbf{i}_\theta = \mathbf{i}_h \times \mathbf{i}_r$ completes the triad.

Denote λ the anomaly of the Sun measured from the X axis in the XY plane. In such a case, the direction of the sunlight and position of the spacecraft are expressed in the body frame $\mathcal{F}_b$, respectively, as

$$\mathbf{u}_S = R_3(\lambda-\varphi)(-\mathbf{i}_{\hat{r}}) = (-\cos(\lambda-\varphi), -\sin(\lambda-\varphi), 0)^\top, \quad \text{and} \tag{17a}$$

$$\mathbf{u}_E = R_3(f+\omega-\varphi)\mathbf{i}_r = (\cos(f+\omega-\varphi), \sin(f+\omega-\varphi), 0)^\top, \tag{17b}$$

where $\mathbf{i}_{\hat{r}}$ is the direction of the position of the Sun in $\mathcal{F}_I$.

A simplified deterministic model

To study the coupled orbit and attitude dynamics it is convenient to understand the attitude dynamics by itself. We do it by first considering a simplified model that assumes that the orbit of the spacecraft is simply Keplerian, and that the apparent motion of the Sun is circular with mean motion $n_\odot$. This will be useful to investigate the possible stable motions when dealing with the complete problem. The simplified equations of motion are

$$\dot{\lambda} = n_\odot, \quad \dot{M} = n, \quad C\ddot{\varphi} = \mathbf{M}_{\rm SRP} + \mathbf{M}_{\rm GG}, \tag{18}$$

where M is the mean anomaly of the spacecraft. The expressions of the torques are those given in Eqs. 8, 11.

Due to the shape of the structure, see Fig. 2, it is important to note that the summand $\mathbf{M}_{\rm SRP}$ has a different representation depending on the orientation φ and the sail aperture α. In order to take this into account and to simplify Eq. 18, it is convenient to consider an the dynamics in a rotating frame that follows the position of the Sun. This is attained by considering the translated coordinates (denoted with $\tilde{\cdot}$)

$$\tilde{\lambda} = \lambda, \quad \tilde{M} = M, \quad \tilde{\varphi} = \varphi - \lambda \quad \text{and} \quad \tilde{\Phi} = \Phi - n_\odot,$$

In these coordinates, if $|\tilde{\varphi}| < \alpha$ the reflective surface of both panels face the sunlight direction, and hence the SRP torque is that provided in Eq. 10; if $\tilde{\varphi} \in (-\pi+\alpha, -\alpha) \cup (\alpha, \pi-\alpha)$ only one of the panels is facing the Sun and hence Eq. 8 should be used instead, and in case $|\tilde{\varphi}| < \pi - \alpha$ the SRP torque is assumed to be zero. See the left panel in Fig. 4. In this sketch, the colored lines represent the sail panels, the dashed line is their bisector (where we assume the bus is located), and the solid colored dot represents the position of the bus.

Also, to provide a unified understanding of the dynamics for a wide range of parameters, it is convenient to introduce a time scaling that reduces the attitude dynamics when the two panels face the sunlight to the product of the cosines. This is achieved by choosing

$$t = t_\star\, s, \qquad t_\star^2 = \frac{m_b + m_s}{A_s} \frac{2C}{a_{1,1}(\eta) p_{\rm SR}}. \tag{19}$$

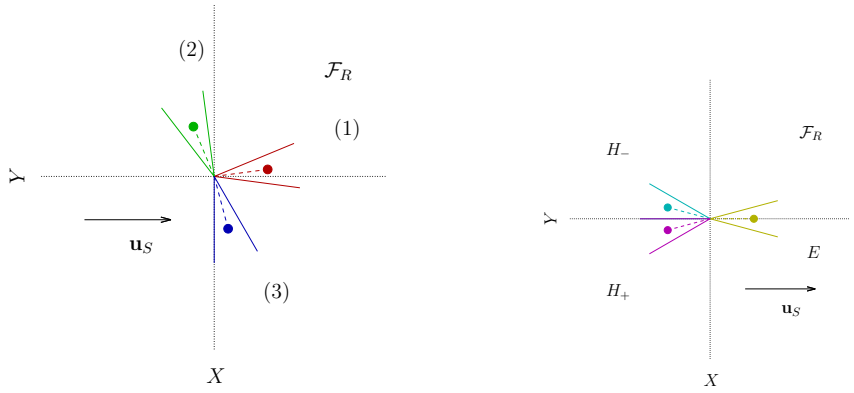

Figure 4. Left: Different orientations of the Sail in the $\mathcal{F}_R$ frame. In red we highlight the panels that produce torque. Right: Schematic depiction of the three equilibria $E, H_\pm$, see the left panel in Fig. 5.

After these changes, Eq. 18 reads

$$\tilde{\lambda}' = t_\star n_\odot, \qquad \tilde{M} = t_\star n, \tag{20a}$$

$$\tilde{\varphi}' = \tilde{\Phi}, \tag{20b}$$

$$\tilde{\Phi}' = \left\{ \begin{array}{lll} \sigma_1\sigma_2 - \frac{a_{2,0}(\eta)}{a_{1,1}(\eta)}\sigma_1^2 - \frac{a_{0,2}(\eta)}{a_{1,1}(\eta)}\sigma_2^2 & \text{if} & \tilde{\varphi} \in (-\pi+\alpha, -\alpha) \\ 2\sigma_1\sigma_2 & \text{if} & \tilde{\varphi} \in (-\alpha, \alpha) \\ \sigma_1\sigma_2 + \frac{a_{2,0}(\eta)}{a_{1,1}(\eta)}\sigma_1^2 + \frac{a_{0,2}(\eta)}{a_{1,1}(\eta)}\sigma_2^2 & \text{if} & \tilde{\varphi} \in (\alpha, \pi-\alpha) \\ 0 & & \text{otherwise} \end{array} \right\} \tag{20c}$$

$$+ \quad t_\star^2 \frac{3\mu}{r^3} \frac{D(\alpha, d)}{C} \gamma_1\gamma_2. \tag{20d}$$

Note that the vector field Eq. 20 is continuous but not differentiable at $\varphi = \pm\alpha$, but it is Lipschitz continuous, so the theorem of existence and uniqueness of solutions of ode applies. In particular, the dynamics in $\tilde{\varphi} \in (-\alpha, \alpha)$ reduce to

$$\ddot{\tilde{\varphi}} = -\sin(2\tilde{\varphi}),$$

that is a mathematical pendulum: its dynamics is described via the Hamiltonian function $\mathcal{H} = \tilde{\Phi}^2/2 - \cos(2\tilde{\varphi})/2$. Moreover, all the periodic orbits of this pendulum are contained in

$$\mathcal{B} = \left\{ (\tilde{\varphi}, \tilde{\Phi}) \text{ such that } |\tilde{\varphi}| < \alpha, \text{ and } |\tilde{\Phi}| < \sqrt{1 - \cos(2\alpha)} \right\}.$$

Outside $\tilde{\varphi} \in (-\alpha, \alpha)$, when only one of the panels is facing the sunlight, we also expect librational motion, but with some impact due to the fact that we pass from one to two panels. It is worth noting that the model given by Eqs. 20 has Hamiltonian structure, with piecewise defined Hamiltonian function, this structure not being restricted only in $\tilde{\varphi} \in (-\alpha, \alpha)$. This will be studied and exploited in forthcoming continuations of the present contribution.

The time scaling Eq. 19 makes sense only if we assure that $a_{1,1}(\eta) \neq 0$. The coefficient $a_{1,1}(\eta)$ vanishes only at

$$d = \frac{w(m_b + m_s)}{2m_b} K(\alpha, \eta), \quad \text{where} \quad K(\alpha, \eta) = \frac{\eta \cos(3\alpha) - \cos\alpha}{2\eta\cos(2\alpha) + \eta + 1}. \tag{21}$$

Note that since $\eta \in (0, 1)$ and $\alpha \in (0, \pi/2)$, $K(\alpha, \eta) < 0$.

Since we are assuming Keplerian motion, r in Eq. 20d is

$$r = \frac{a\sqrt{1 - e^2}}{1 + e\cos f},$$

Using this relation, Eq. 20d reads

$$\delta P(\alpha, d)\gamma_1\gamma_2(1 + e\cos f)^3, \quad \text{where} \quad \delta = \frac{1}{a^3\sqrt{(1 - e^2)^3}},\ P(\alpha, d) = 3\mu t_\star^2 \frac{D(\alpha, d)}{C}. \tag{22}$$

Since $\gamma_1 = \cos(f + \omega + \tilde{\lambda} - \tilde{\varphi})$ and $\gamma_2 = \sin(f + \omega + \tilde{\lambda} - \tilde{\varphi})$, see Eq. 17b, the gravity-gradient is generically a quasi-periodic perturbation, where the perturbation size is proportional to the inverse cube of the semi-major axis of the orbit.

Unperturbed dynamics Consider Eq. 20 without the gravity gradient effect, that is, ignoring Eq. 20d. As commented above, if we only consider the SRP torque the dynamics do not depend on the orbit the ode reduces to study the dynamics solely on $(\tilde{\varphi}, \tilde{\Phi})$. It is clear that there are three distinctive equilibria that are located at

$$H_\pm = (\pm\pi \mp \alpha, 0) \quad \text{and} \quad E = (0, 0),$$

which correspond to motion initially with the same angular velocity of the apparent motion of the Sun, and oriented towards it, as shown in Fig. 4, right. Note that also all initial configurations initially at $(\tilde{\varphi}_0, \tilde{\Phi}_0)$ with $\tilde{\Phi}_0 = 0$ and $\tilde{\varphi}_0 \in (\pi - \alpha, \pi + \alpha)$ are also equilibria of the system, but these are regarded as virtual since they would cease to be equilibria under any small perturbation.

Concerning the stability of the equilibria, $H_\pm$ are unstable regardless of the values of the parameter. On the other hand, the equilibrium E is stable only if

$$a_{1,1}(\eta) < 0 \quad \Leftrightarrow \quad d > \frac{w(m_b + m_s)}{2m_b} K(\alpha, \eta), \tag{23}$$

see Eq. 21. In right panel of Fig. 5 we depict the right hand side inequality of Eq. 23 for the values of w, m_b and m_s of $\mathtt{SC}_1$ and $\mathtt{SC}_2$. The ordinates indicate the minimum value of d measured in meters so that the sun-pointing attitude is stable, for different values of the reflectance η. If we come back to Fig. 3, this indicates the positions of the bus on $y = 0$ in $\mathcal{F}_b$ that make the orientation E stable. Note that, since $K(\alpha, \eta) < 0$, in particular, all positions of the bus in front of the sail (e.g. all three sketches in Fig. 3) have E as stable equilibrium.

In the left panel of Fig. 5 we display the propagation of some unperturbed orbits of $\mathtt{SC}_1$ up to $s = 30$ (that corresponds to a dimensional time of 4.44 min), where we see that the phase space of Eq. 20 resembles that of a pendulum: around the stable equilibrium E in a region bounded by the separatrices of $H_\pm$ the dynamics is librational. The vertical dotted lines located at $\tilde{\varphi} = \pm\alpha$ indicate

the regions where one or two panels are facing the sunlight. A similar qualitative figure is obtained if we consider $\mathtt{SC}_2$ instead.

It is remarkable that there is a non-negligible region of stable librational attitude dynamics around the sun-pointing attitude E. Without any perturbation, any displayed configuration would librate around it indefinitely.

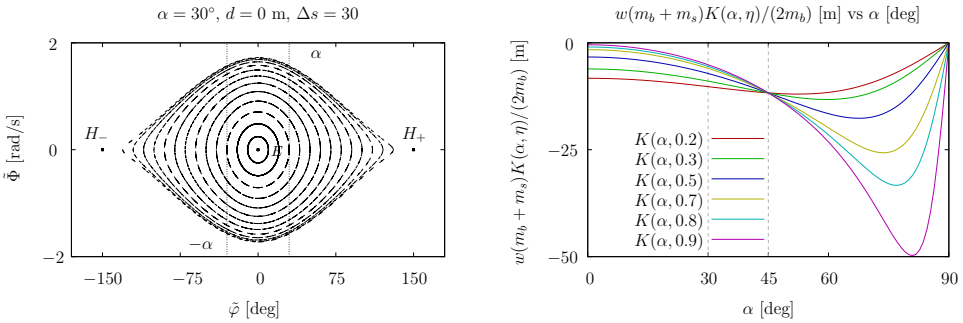

Figure 5. Left: Phase space of Eq. 20 for $\varepsilon = 0$ in $(\tilde{\varphi}, \tilde{\Phi})$ of $\mathtt{SC}_1$. The vertical dotted lines indicate the change of regimes. Continuous (resp. dashed) lines correspond to dynamics where 2 (resp. 1) sail panels produces torque. Right: Depiction of the necessary condition for the stability of the sun-pointing attitude.

Perturbed motion If we consider the full differential equation Eq. 20, where all the cosines in Eq. 17 appear, we can no longer ignore the effects of the anomalies λ and f that appear in the perturbation term Eq. 20d. The physical meaning of the perturbed motion is the study of the effect of considering an asymmetrical spacecraft, and in particular the assessment of the effect of displacing the centre of mass of the structure by adding the bus. Namely, as commented above, the gravity gradient torque introduces a quasi-periodic effect on the system.

In such situation, in the full 4D ode, the unperturbed invariant objects "gain" the non-resonant frequencies of the perturbation.[14] In particular, under the perturbation, E becomes, generically, a 2D quasi-periodic torus with frequencies n and $n_\odot$. What is of interest in our problem is that periodic orbits of the unperturbed system can become 3D invariant tori that separate space, since they are of co-dimension 1. That is, under the gravity gradient perturbation some stable or practically stable motion can survive.

It is important to note that some of this structure is also expected to be destroyed, but initial conditions in librational motion in the unperturbed case can become eventually rotational once the perturbation is added. If the sail that is initially in $|\tilde{\varphi}| < \pi - \alpha$ reaches $|\varphi| > \pi - \alpha$ with nonzero angular velocity, this rotational state will never be lost. Hence it makes sense to consider these orbits as eventually *tumbling*. From a practical point of view, this defines an *escaping criterion*: the trajectory of an initial condition is considered to be uncontrolled if it reaches a state $|\tilde{\varphi}| > \pi - \alpha$ with nonzero angular velocity.

The smallness of the perturbation is key to be able to ensure the persistence of tori and hence the existence of stable attitude dynamics. And this, in turn, depends on the values of α and d via the factor $P(\alpha, d)$ in Eq. 22. The full dependence on these parameters is contained in the quotient $D(\alpha, d)/a_{1,1}(\eta)$, and it is easy to see that, for the values where $a_{1,1}(\eta) > 0$, that is, when the

orientation of the spacecraft towards the Sun is stable, for a fixed value of α, as a function of d, the quotient (and hence $P(\alpha, d)$) is strictly convex and has an absolute minimum. In Fig. 6, left, we display some examples of $P(\alpha, d)$ for fixed values of α.

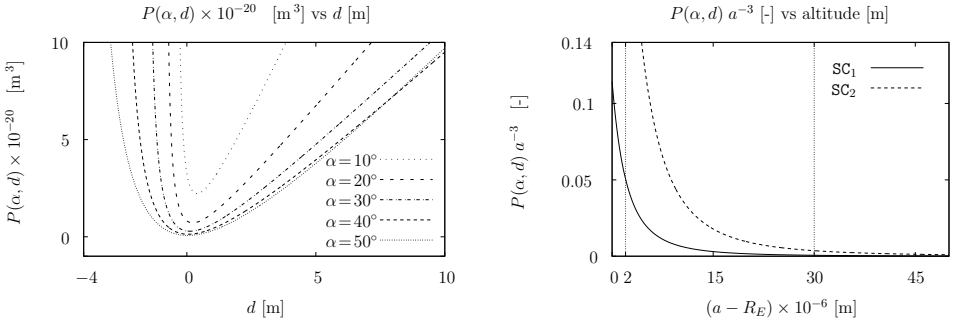

Figure 6. Left: Size of the perturbation, $P(\alpha, d)$, see Eq. 22. Here we display curves for fixed $\alpha = 10, 20, 30, 40$ and 50 deg. In the bottom left corner we indicate the corresponding value of our test example. Right: $P(30, 0)/(R_E + a')^3$, where a' is the altitude of the orbit.

In the right panel of Fig. 6 we display how does the perturbation size depend on the altitude of the orbit for $\mathtt{SC}_1$ and $\mathtt{SC}_2$. The vertical dashed lines indicate the separations from Low Earth Orbits (LEO) and Medium Earth Orbits (MEO) at $a' = 5000$ km, and between MEO and the geostationary region (GEO) at $a' = 35000$ km.

Detection of stable attitude dynamics in the perturbed setting Under the presence of the perturbation, the dynamical objects of our interest are replaced to tori of dimension 2 and 3. Despite the techniques for the approximation of these objects are standard nowadays they are of no interest for the purpose of this paper, but only a justification of the existence of stable motions in the perturbed setting.

Note that the Keplerian orbit in $\mathcal{F}_I$ is fixed, but in the rotational frame $\mathcal{F}_R$ the argument of the perigee ω changes as a function of time: $\tilde{\omega} = \omega - \lambda$. Also note that the two additional frequencies of the perturbation have significatively different orders of magnitude, namely $n_\odot \ll n$, so the change in ω is very slow. This leads us to, instead of considering the full continuous model, to discretize it according to the frequency of f, that since the motion is assumed to be fixed Keplerian, is $n = \sqrt{\mu a^{-3}}$.

More concretely, we detect stable motions as stable orbits of what we will refer to as the *return-to-perigee map* (RTPM): for a fixed Keplerian orbit, with fixed a, e and initial $\omega = \omega_0$, we propagate the orbit starting at the perigee $f = 0$, assuming that the attitude of the satellite is initially in the range of $(\tilde{\varphi}, \tilde{\Phi})$ indicated in the left panel of Fig. 5. Along the integration, we only save the states where f is a multiple of 2π, that is, the states at the perigee. Note that this is a Poincaré stroboscopic map at time $t = 2\pi/n$. For each initial condition we propagate the orbit until we reach `itmax` iterates or the orbit becomes tumbling, that is, if $|\tilde{\varphi}| > \pi - \alpha$.

The problem depends on many parameters and it is not possible to provide with full account of the possible dynamics. Here we illustrate the stable attitude states for $\mathtt{SC}_{1,2}$ for orbits in an altitude $a' = 5000$ km, with eccentricities $e = 0.001$ and 0.1, computing at most `itmax` iterates. The reason

for these choices is that for higher altitudes not only the computation of iterates of the RTPM is increasingly expensive, but also the perturbation size is smaller, so the obtained dynamics are close to that shown in the left panel of Fig. 5. For smaller altitudes the range of feasible eccentricities decreases, so a comparative study is of less value.

The results for $e = 0.001$ and 0.1 can be found in Figs. 7 and 8, respectively. In each of this panels we display the $(\tilde{\varphi}, \tilde{\Phi})$ plane, and mark straight lines at $\tilde{\varphi} = \pm\alpha$. These bound the vertical region where the dynamics is due to a single panel or to both panels at the same time. It is worth noting that in all cases there is a central stable orientation, which is roughly at $(0, 0)$. In the results for $\mathtt{SC}_2$ it is visible that this equilibrium is slightly displaced due to the gravity-gradient torque perturbation. The important feature of all shown panels is that they all have orbits of the RTPM on what seems to be an invariant curve, and hence correspond to stable motion. In the global picture these are orbits either on or very close to 3D tori that separate space and hence bound stable attitude dynamics.

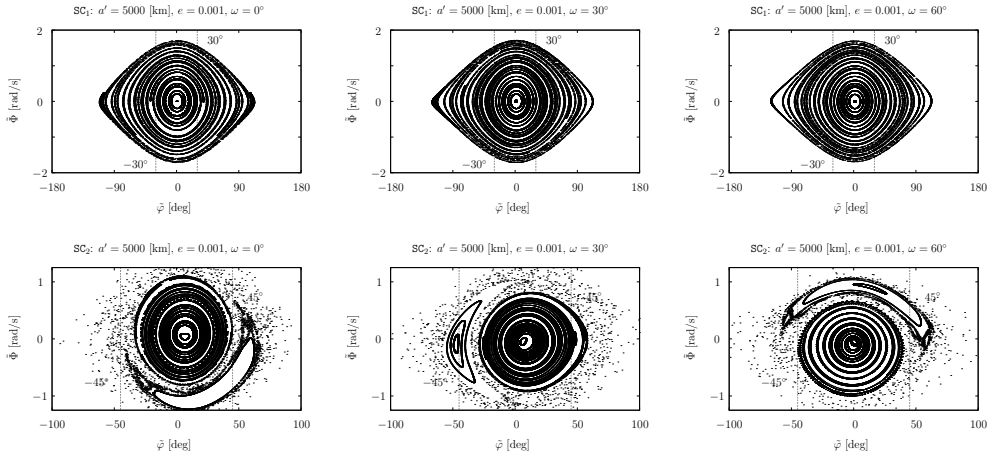

Figure 7. Phase space of the RTPM for $e = 0.001$. Top: results for $\mathtt{SC}_1$. Bottom: results for $\mathtt{SC}_2$. From left to right: $\omega = 0°, 30°$ and $60°$.

Note the similarity between the left panel of Fig. 5 and the phase spaces for $\mathtt{SC}_1$ where we only show librational motion: for the proposed structure, since the centre of mass of both the bus and panels is located at the origin, the perturbation does not seem to affect much the overall dynamics of the spacecraft. The most visible change as we change ω is that the left tip of the librational zone is seems to move towards the left. Non displayed results for $\tilde{\omega} \in (\pi/2, \pi)$ show that this behaviour is translated to the right in these cases. Note that despite the great resemblance with the non-perturbed case, one can see discrepancies. Say, for instance, in Fig. 7 top right, the outermost 'curve' displays some thickness, which may correspond to confined chaotic motion; or in Fig. 7 top left, where some points close to the stable orientation look as dashed, which correspond to higher order resonant motion between SRP and gravity gradient.

On the contrary, the results for the structure $\mathtt{SC}_2$ show that most of the stable motion is restricted to the region where both panels face the Sun, with some interesting features. On the one hand, there seems to have appeared another stable equilibrium orientation, that is surrounded also by an island-like structure. This may account for an orientation where the displacement between centres of mass

gives rise to a compensation of SRP and gravity gradient. Also, note that this equilibrium rotates as the initial $\tilde{\omega}$ changes. This is mainly due to the fact that for different $\tilde{\omega}$ the spacecraft spends more or less time close to the Earth in a certain orientation where the previous compensation occurs. All points on what appear to be continuous curves correspond to librational motion, while the "dust" regions correspond to motion that starts being librational but becomes tumbling after some transient.

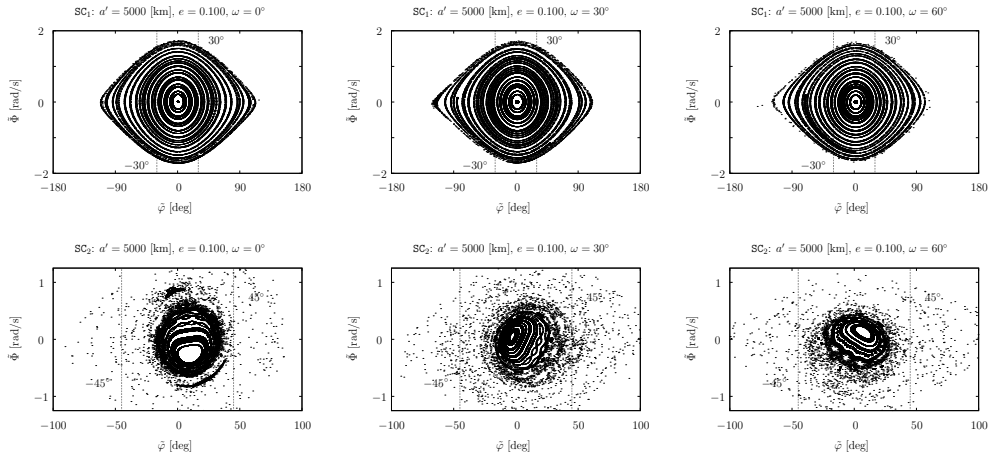

Figure 8. Phase space of RTPM for $e = 0.100$. Top: results for $\mathtt{SC}_1$. Bottom: results for $\mathtt{SC}_2$. From left to right: $\omega = 0^\circ, 30^\circ$ and 60°.

It seems that this second equilibrium is destroyed for $e = 0.1$, see the bottom panels in Fig. 8. In the leftmost plot we see that there are some islands that can be remnants of the previous large island. Note that the one in the top has undergone what seems a 1:3 resonance in section. Again, as in the other plots the whole island seems to rotate as ω changes, but also changing the overall structure of the island.

Validation of the results in the complete problem To check the validity of the obtained results with the simplified attitude model we have propagated some orbits of Eq. 18 coupled with Eqs. 16. The position of the Sun is retrieved from the NASA SPICE toolkit. Since the coupled dynamics has two different time scales, the propagation time increases significatively. To overcome the stiffness of the equations, we have used an implicit Runge-Kutta-Gauss method of order 4.

We have chosen a, e as above, $\omega_0 = 0^\circ$, and attitude states initially parallel to the Earth-Sun vector and initial angular velocity $\Phi = n_\odot$, where $n_\odot$ is computed at each integration step. We have computed 250 iterates ($\approx$ 40 days of integration) of the RTPM for each initial condition considered. Here the integrations are performed in the $\mathcal{F}_{\mathrm{t,n,h}}$ frame, while the study of the simplified deterministic model was performed in $\mathcal{F}_b$. To be able to compare with the results shown in Figs. 7 and 8, we have to plot, in the abscissas $\varphi - \lambda$, and in the ordinates $t_\star(\Phi - n_\odot)$. The results of the propagation are shown in Fig. 9.

Each color in each panel of Fig. 9 represents the propagation of the same initial condition. The shown results show, for $\mathtt{SC}_1$, a very similar behaviour to that of the simplified model: a phase space that resembles that of a pendulum. We have chosen the same initial conditions for the two different values of the eccentricity. The discrepancies are due to the fact that in both situations the same

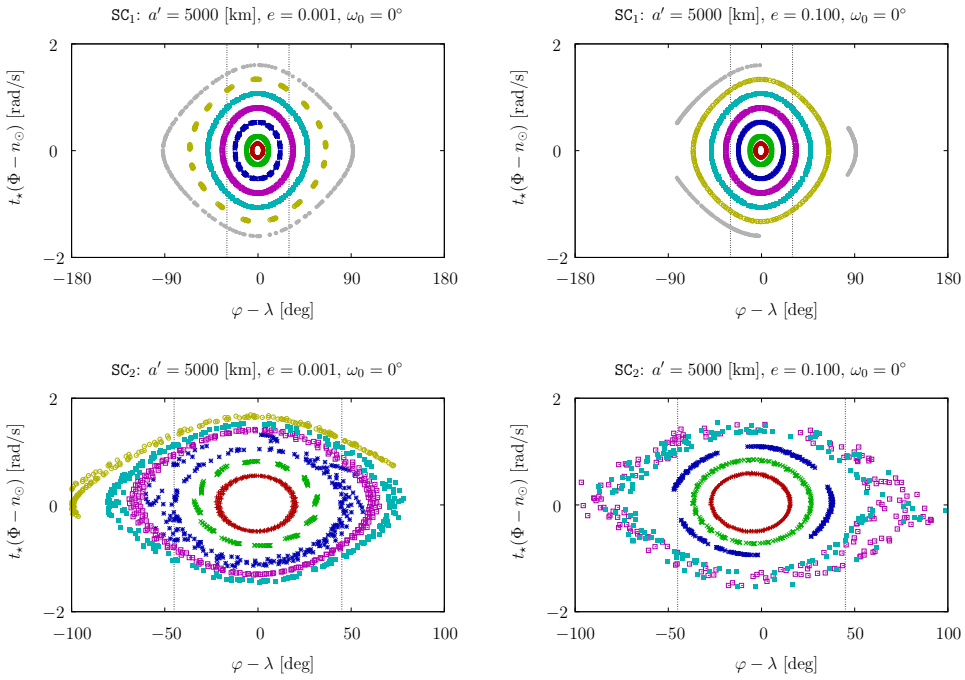

Figure 9. Phase space of the RTPM in the complete problem. Top: results for $\mathtt{SC}_1$. Bottom: results for $\mathtt{SC}_2$. From left to right: $e = 0.001, 0.100$.

initial condition is on a different torus, that has different frequencies. But also here in the more complete problem the attitude seems to be stable if starts close to a sun-pointing attitude.

Concerning the results for $\mathtt{SC}_2$, again, most of what seems to be stable motion is within the region where both panels reflect sunlight at the same time. Note that here orbits outside this region seem to diffuse strongly towards uncontrolled motion. Namely, the same initial conditions that do not escape for 250 iterates for $e = 0.001$ do escape for $e = 0.1$.

The problem of eclipses The fact that we are restricting ourselves to a planar problem forces us to study the effect of eclipses. Here again the different time scales between orbit and attitude dynamics produces an unavoidable effect: except for attitudes at or extremely close to the sun-pointing orientation with angular velocity also extremely close to $n_\odot$ an orbit becomes uncontrollable with probability 1. As commented in the introduction, in[10] the authors attack this problem by considering a moderate spin of the QRP structure. This line of thought will be studied in future contributions.

STABILIZING PROPERTIES IN A DRAG-DOMINATED REGION

Taking into account the similarity between the explicit representation of the torques due to SRP and atmospheric drag, compare Eqs. 8 and 13, one may be tempted to perform a similar study as that performed by SRP but with the corresponding expressions for the drag instead. But one has to notice that, contrary to the SRP case, the only-drag attitude dynamics depends explicitly on the orbit via the density ρ and the relative velocity v_{rel}.

Yet it is still interesting to provide the explicit equations so that we can study the stability of the tangent-to-orbit orientation. Namely, proceeding as for the SRP, we need to write $\mathbf{u}_E$ (see Eq. 17b) and $\mathbf{u}_{\rm rel}$ in the $\mathcal{F}_b$ frame. The latter reads

$$\mathbf{u}_{\rm rel} \;=\; R_3(\psi)(-\mathbf{i}_{\rm t}) = (-\cos\psi, -\sin\psi, 0)^\top, \psi = f - \beta + \pi/2 - \varphi, \tag{24}$$

where β is the flight path angle: that between the velocity vector and the local horizontal. Note that for circular orbits $\beta = 0$.

Similarly to the SRP case, the attitude dynamics in a drag-dominated region are given by

$$\dot\lambda = n_\odot, \quad \dot M = n, \quad C\ddot\varphi = \mathbf{M}_{\rm drag} + \mathbf{M}_{\rm GG}. \tag{25}$$

Here we assume altitudes that are below 1000 km.

Proceeding exactly as we did in the previous section, to have a global picture of the dynamics it is convenient to consider a time scale that simplifies the representation of the motion when the two panels produce torque. Here, since ρ and $v_{\rm rel}$ depend on the position of the orbit, we have to consider

$$t = t_{\star\star} s, \qquad t_{\star\star}^2 = \frac{m_b + m_s}{A_s}\frac{4C}{C_D b_{1,1}}. \tag{26}$$

Then, since the drag acceleration has direction $(-1,0,0)^\top$ in $\mathcal{F}_{\rm t,n,h}$, it is convenient to consider the translated coordinates (denoted with $\hat{\cdot}$)

$$\hat M = M, \quad \hat\beta = \beta, \quad \hat\varphi = \varphi - f + \beta - \frac{\pi}{2}, \quad \hat\Phi = \Phi - \frac{1}{1+e\cos f}\frac{df}{dt}$$

in which the attitude dynamics read

$$\hat\varphi' \;=\; \hat\Phi, \tag{27a}$$

$$\hat\Phi' \;=\; \rho v_{\rm rel}^2 \left\{ \begin{array}{ll} \nu_1\nu_2 - \frac{b_{2,0}}{b_{1,1}}\nu_1^2 - \frac{b_{0,2}}{b_{1,1}}\nu_2^2 & \text{if} \quad \hat\varphi \in (-\pi+\alpha, -\alpha) \\ 2\nu_1\nu_2 & \text{if} \quad \hat\varphi \in (-\alpha, \alpha) \\ \nu_1\nu_2 + \frac{b_{2,0}}{b_{1,1}}\nu_1^2 + \frac{b_{0,2}}{b_{1,1}}\nu_2^2 & \text{if} \quad \hat\varphi \in (\alpha, \pi-\alpha) \end{array} \right\} \tag{27b}$$

$$-t_{\star\star}^2 \frac{d}{dt}\left(\frac{1}{1+e\cos f}\frac{df}{dt}\right) + t_{\star\star}^2 \frac{3\mu}{r^3}\frac{D(\alpha,d)}{C}\gamma_1\gamma_2. \tag{27c}$$

The similarity between Eqs. 27 and Eqs. 20 is remarkable, the first summand in Eq. 27c being the main difference. This accounts for the effect of the motion along an elliptic orbit. Note that in case the motion took place in a fixed Keplerian orbit, both summands of Eq. 27c would be a perturbation with the same frequency, the mean motion n.

Note that if ρ and $v_{\rm rel}$ were constant, the unperturbed circular motion would be the same as in the SRP and gravity-gradient case. This suggests to translate the concept of *tumbling* spacecraft we introduced before in this context: in the drag dominated zone a spacecraft is controlled if $|\hat\varphi| < \pi - \alpha$. This corresponds to cases where either one or two panels face the atmosphere from the front.

Also if ρ and $v_{\rm rel}$ were constant, the dynamics in the interval $|\hat\varphi| < \alpha$ would be that of a mathematical pendulum, and taking into account the constant in front of the expressions Eq. 13 and the

fact that $\nu_1 = -\cos\hat{\varphi}$ and $\nu_2 = \sin\hat{\varphi}$, the stability of the tangent-to-orbit orientation, with the velocity $\beta' - f'$ relies solely on the fact that the coefficient $b_{1,1}$ is positive. This condition reads

$$b_{1,1} = a_{1,1}(0) < 0 \quad \Leftrightarrow \quad d > \frac{w(m_b + m_s)}{2m_b} K(\alpha, 0), \tag{28}$$

to be compared with Eq. 23. This is also a necessary condition for the stability of the spacecraft related to that seen before in the SRP-dominated case. In Fig. 10 we depict the condition in the right-hand-side of Eq. 28 for for the values of w, m_b and m_s of $\mathtt{SC}_1$ and $\mathtt{SC}_2$. The shown line corresponds to the minimal distance d for which there is stability of the tangent-to-orbit orientation of the sail. As before in the SRP-dominated case, these include, in particular, all positions of the bus in front of the sail an permit even positions behind it, always containing that of $\mathtt{SC}_1$, where both bus and sail structure have the centre of mass in the very same point.

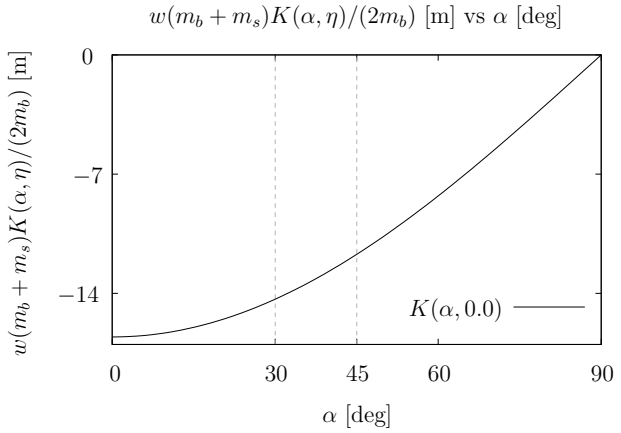

Figure 10. Necessary conditions for the stability of the tangent-to-orbit orientation of the sail in drag-dominated regions.

Results in the complete problem

To assess the auto-stabilizing properties we have considered $c_D = 2.2$ and we have retrieved the atmospheric density using an exponential model, see Appendix B in[15] to propagate initial conditions in the complete attitude (with drag and gravity-gradient torques) and orbit (with drag and J_2 accelerations) model. For altitudes above 500 km, stable attitude dynamics can be observed together with a slow (compared with the attitude) decrease of the semi-major axis a due to the drag acceleration, as expected.

In our simulations we observed that the minimum atmosphere density to stabilize such spacecrafts is around 800 km of altitude. Above that, the spacecrafts become rapidly uncontrolled, as the gravity-gradient perturbation dominates.

Below 800 km of altitude the drag torque dominates and stabilization occurs, and we obtain qualitatively similar results to those in the SRP case. For a better visualization results for altitudes below 500 km are here shown, where the semi-major axis of the orbits decreases more rapidly. To

exemplify the observed dynamics, Fig. 11 shows the iterates of the RTPM for trajectories initially at an altitude $a = R_E + 500$ km, eccentricity $e = 0.001$ and as above $\omega_0 = 0$; and with attitude initially pointing towards the velocity vector and with small Φ, close to $d(\beta - f)/dt$. These initial conditions were propagated either until the spacecraft was uncontrollable or if $a < R_E + 250$ km. This corresponds, for each initial condition, to around 150 iterates of the RTPM.

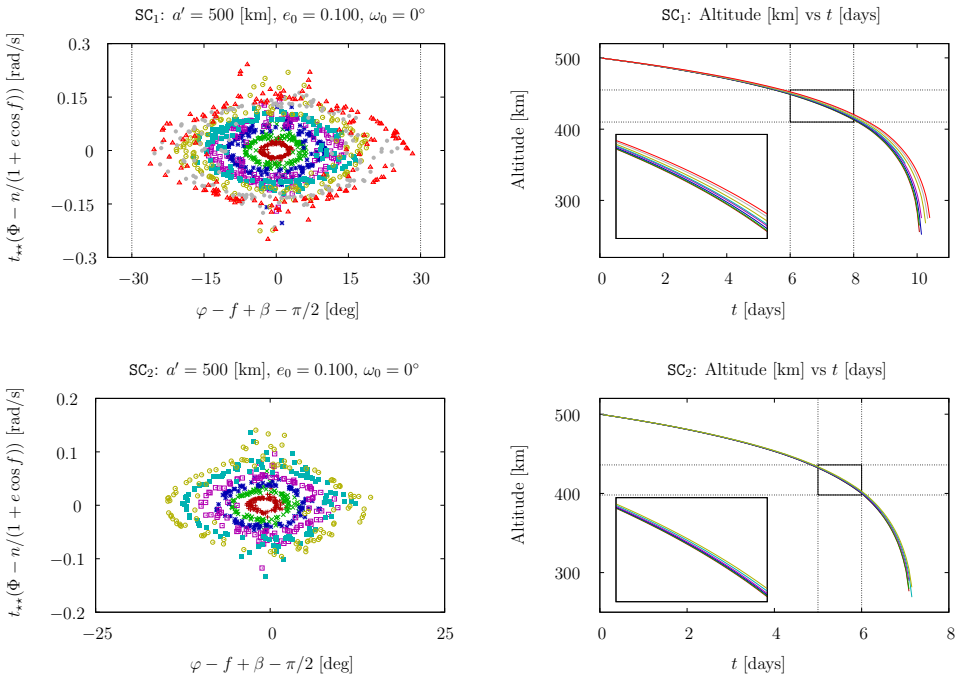

Figure 11. Left: Phase space of the RTPM in the complete problem with drag and gravity gradient torques. Right: Variation of the altitude of the orbit. Top: results for $\mathtt{SC}_1$. Bottom: results for $\mathtt{SC}_2$.

In the left panels of Fig. 11 we show the phase space of the attitude dynamics of $\mathtt{SC}_1$ and $\mathtt{SC}_2$. In the abscissas the difference between ψ, as defined in Eq. 24, and in the ordinates we show the difference between Φ and $d(\beta - f)/dt$ is displayed. The right plot show how does the altitude of the orbit vary, as a function of time, expressed in days starting from the initial integration time. The different colors indicate different initial conditions, and the same colors in the left and right panels indicate that the results correspond to the same trajectory. It is important to remark that all the displayed orbits maintained the controlled property during the whole studied motion. We do not display any uncontrolled orbit, and all of them appeared to be outside the region in the phase space displayed in the left plots, that is, further from the tangent-to-orbit attitude.

For both spacecraft examples, $\mathtt{SC}_1$ and $\mathtt{SC}_2$, in the phase space we see that all orbits are contained within $|\hat{\varphi}| < \alpha$, that is, when both panels produce torque and acceleration due to the drag force. Remark that as in the SRP case, the spacecraft $\mathtt{SC}_2$ has worse stability results which can be attributed to the fact that $d \neq 0$. We observe that the orbit seems to be more regular if we start closer to the tangent-to-orbit orientation, and that this attitude is conserved throughout the whole motion until

$R_E + 250$ km. Orbits initially further from this equilibrium attitude tend to oscillate more, but some still maintain the stable attitude. Here points in the same trajectory seem to fill a larger set in a phase space resembling a thicker cloud of points. This can be attributed to the rapid change of Keplerian elements of the orbit, compared to the SRP case.

Concerning the variation in altitude, for both spacecrafts, if the motion starts closer to the tangent-to-orbit attitude, the deorbiting is faster. See the zooms in the right panels.

SUMMARY OF RESULTS AND CONCLUSIONS

In this work we have dealt with a planar reduction of the coupled orbit and attitude dynamics of a solar sail with helio-stable properties. We have considered a simplified spacecraft design that consists of 2 reflective panels of aperture angle α and a bus with variable position of its centre of mass d. This has allowed to establish a simplified deterministic model of the attitude dynamics when considering SRP and gravity gradient torques. With this we have been able to

1. Check the stability of the sun-pointing attitude, and to perform a sensitivity analysis with respect to α and d. This provides indications on how to position the bus with respect to the sail structure. Among the possible options we highlight that spacecrafts with the bus behind the sail at its centre of mass, and spacecrafts with the bus at the tip of the sail are stable at the sun-pointing orientation.

2. Detect regions of stable attitude dynamics close to the sun-pointing attitude. The libration regions are at most $2(\pi - \alpha)$ radians wide. The discrepancies due to considering different spacecraft configurations have been studied, showing that the most robust orientations are those where both panels are facing the sun light.

3. Validate the results in a complete planar orbit and attitude model, taking into account SRP and J_2 accelerations in the orbit dynamics. The previous study of the deterministic model allowed to study which initial attitude states were adequate (both orientation and angular velocity) to get helio-stable orientations that appeared to be conserved along the motion if close enough to the sun-pointing attitude.

After this, taking into account the similarities between drag and SRP forces, the dynamics of a similar sail in a drag-dominated region has been studied. The stability of the tangent-to-orbit attitude has been established similarly to that of the sun-pointing attitude in the SRP case. The nature of the drag force forced us to study directly the problem in the full orbit and attitude model. We have observed numerically that drag force is enough to stabilize a spacecraft as those considered below 800 km of altitude. Below this threshold, regions of practical stability close to the tangent-to-orbit attitude have been detected, and examples of deorbiting satellites using drag without any attitude control have been provided.

There are a number of future lines of research that emerge from this work. Among them we should highlight first to perform a complete numerical study of the planar problem for some spacecrafts of interest. This may allow to combine the SRP and drag effects to deorbit satellites,[16] but exploiting the auto-stabilizing properties of the family of sails under consideration to reduce as much as possible the need for attitude control. And of course the performance of a similar study as the present one but considering the motion of the 3D QRP as suggested in.[8]

ACKNOWLEDGEMENTS

The research leading to these results has received funding from the Horizon 2020 Program of the European Unions Framework Programme for Research and Innovation (H2020-PROTEC-2015) under REA grant agreement number 687500 ReDSHIFT. The support of J. Gimeno and M. Jorba-Cuscó is also acknowledged.

REFERENCES

[1] Y. Tsuda, O. Mori, R. Funase, H. Sawada, T. Yamamoto, T. Saiki, T. Endo, and J. Kawaguchi, "Flight status of IKAROS deep space solar sail demonstrator," *Acta Astronautica*, Vol. 69, No. 9, 2011, pp. 833 – 840, https://doi.org/10.1016/j.actaastro.2011.06.005.

[2] L. Johnson, M. Whorton, A. Heaton, R. Pinson, G. Laue, and C. Adams, "NanoSail-D: A solar sail demonstration mission," *Acta Astronautica*, Vol. 68, No. 5, 2011, pp. 571 – 575. Special Issue: Aosta 2009 Symposium, https://doi.org/10.1016/j.actaastro.2010.02.008.

[3] C. Colombo, A. Rossi, F. Dalla Vedova, V. Braun, B. Bastida-Virgili, and H. Krag, "Drag and Solar Sail deorbiting: re-entry time versus cumulative collision probability," *International Astronautical Congress*, No. IAC-17-A6.2.8, 2017.

[4] C. Colombo and T. de Bras de Fer, "Assessment of passive and active solar sailing strategies for end of life re-entry," *International Astronautical Congress*, No. IAC-16-A6.4.4, 2016.

[5] J. A. Borja and D. Tun, "Deorbit Process Using Solar Radiation Force," *Journal of Spacecraft and Rockets*, Vol. 43, No. 3, 2006, pp. 685–687, 10.2514/1.28765.

[6] C. Lücking, C. Colombo, and C. R. McInnes, "A passive satellite deorbiting strategy for MEO using solar radiation pressure and the J_2 effect," *Acta Astronautica*, Vol. 77, 2012, pp. 197–206.

[7] C. Lücking, C. Colombo, and C. R. McInnes, "Solar Radiation Pressure-Augmented Deorbiting: Passive End-of-Life Disposal from High-Altitude Orbits," *Journal of Spacecraft and Rockets*, Vol. 50, 11 2013.

[8] M. Ceriotti, P. Harkness, and M. McRobb, "Variable-geometry solar sailing: the possibilities of quasi-rhombic pyramid," *Advances in Solar Sailing* (M. McDonald, ed.), Springer, 2013.

[9] L. Felicetti, M. Ceriotti, and P. Harkness, "Attitude Stability and Altitude Control of a Variable-Geometry Earth-Orbiting Solar Sail," *Journal of Guidance, Control, and Dynamics*, Vol. 39, No. 9, 2016, pp. 2112 – 2126.

[10] L. Felicetti, P. Harkness, and M. Ceriotti, "Attitude and orbital dynamics of a variable-geometry, spinning solar sail in Earth orbit," *The Fourth International Symposium on Solar Sailing 2017 17th - 20th January, 2017, Kyoto, Japan*, 2017, pp. 1–10.

[11] F. Markley and J. Crassidis, *Fundamentals of Spacecraft Attitude Determination and Control*. Space Technology Library, Springer New York, 2014.

[12] R. Battin, *An Introduction to the Mathematics and Methods of Astrodynamics*. AIAA education series, American Institute of Aeronautics & Astronautics, 1999.

[13] F. Dalla Vedova, P. Morin, T. Roux, R. Brombin, A. Piccinini, and N. Ramsden, "Interfacing Sail Modules for Use with Space Tugs ," *Aerospace*, Vol. 5, No. 48, 2018.

[14] À. Jorba and J. Villanueva, "On the Persistence of Lower Dimensional Invariant Tori under Quasi-Periodic Perturbations," *Journal of Nonlinear Science*, Vol. 7, 10 1997.

[15] D. Vallado and W. McClain, *Fundamentals of Astrodynamics and Applications*. Space Technology Library, Microcosm Press, USA, fourth ed., 2013.

[16] V. Stolbunov, M. Ceriotti, C. Colombo, and C. R. McInnes, "Optimal Law for Inclination Change in an Atmosphere Through Solar Sailing," *Journal of Guidance, Control, and Dynamics*, Vol. 36, No. 5, 2013, pp. 1310 – 1323, 10.2514/1.59931.